Geophysical Research Letters

RESEARCH LETTER
10.1029/2020GL088580

Crustal Deformation in Southern California Constrained by Radial Anisotropy From Ambient Noise Adjoint Tomography

Kai Wang[1,2], Chengxin Jiang[3,4], Yingjie Yang[2], Vera Schulte-Pelkum[5], and Qinya Liu[1,6]

[1]Department of Physics, University of Toronto, Toronto, Ontario, Canada, [2]Department of Earth and Planetary Sciences, Macquarie University, Sydney, New South Wales, Australia, [3]Now at Research School of Earth Science, The Australian National University, Canberra, ACT, Australia, [4]Department of Earth and Planetary Sciences, Harvard University, Cambridge, MA, USA, [5]Cooperative Institute for Research in Environmental Sciences and Department of Geological Sciences, University of Colorado Boulder, Boulder, CO, USA, [6]Department of Earth Sciences, University of Toronto, Toronto, Ontario, Canada

Key Points:
- A radially anisotropic shear wave velocity model of Southern California is constructed from ambient noise adjoint tomography
- Positive radial anisotropy in the crust is caused by subhorizontal alignment of mica and amphibole associated with extensional tectonics
- Negative anisotropy west of the San Andreas Fault is attributed to steeply dipping amphibole schists or subhorizontally foliated plagioclase

Supporting Information:
- Supporting Information S1

Correspondence to:
K. Wang and C. Jiang,
wangkaim8@gmail.com;
chengxinjiang@gmail.com

Citation:
Wang, K., Jiang, C., Yang, Y., Schulte-Pelkum, V., & Liu, Q. (2020). Crustal deformation in Southern California constrained by radial anisotropy from ambient noise adjoint tomography. *Geophysical Research Letters*, *47*, e2020GL088580. https://doi.org/10.1029/2020GL088580

Received 25 APR 2020
Accepted 4 MAY 2020
Accepted article online 4 JUN 2020

Abstract We build a new radially anisotropic shear wave velocity model of Southern California based on ambient noise adjoint tomography to investigate crustal deformation associated with Cenozoic evolution of the Pacific-North American plate boundary. Pervasive positive radial anisotropy (4%) is observed in the crust east of the San Andreas Fault (SAF), attributed to subhorizontal alignment of mica/amphibole foliation planes resulting from significant crustal extension. Substantial negative anisotropy (6%) is revealed in the middle/lower crust west of the SAF, where high shear wave speeds are also observed. The negative anisotropy could result from steeply dipping amphibole schists in a shear zone developed during Laramide flat slab subduction. Alternatively, it could be caused by the crystal preferred orientation (CPO) of plagioclase, whose fast axis aligns orthogonally to a presumed subhorizontal foliation. The latter new mechanism highlights potentially complex CPO patterns resulting from different lithospheric mineralogy, as suggested by laboratory experiments on xenoliths from the region.

Plain Language Summary The crust of Southern California has been shaped by complex tectonic processes through the evolution of the Pacific-North America plate boundary. The mechanisms of crustal deformation in this area are not fully understood. We investigate the deformation regime by studying the seismic radial anisotropy of shear wave speed associated with mineral or structural orientations. Our work reveals pervasive positive radial anisotropy ($V_{SH} > V_{SV}$) in the crust and uppermost mantle, which is consistent with the tectonic setting of widespread and long-term crustal extension of the western United States through the Cenozoic. Interestingly, we also observe strong negative anisotropy ($V_{SH} < V_{SV}$) in the lower crust west of the San Andreas Fault that has not been reported before. We interpret the positive anisotropy to be caused by the subhorizontal alignment of foliation planes of mica/amphibole whereas the negative one is potentially created by either steeply dipping amphibole schists or subhorizontal alignment of plagioclase. The distinct radial anisotropies across the transform plate boundary might indicate the importance of complex CPO patterns, resulting from different lithospheric mineralogy under the same strain regime.

1. Introduction

Situated at the Pacific-North American plate boundary, Southern California has experienced a complex tectonic evolution over the past 200 million years (Burchfiel & Davis, 1972), which has shaped its present-day lithospheric structure (e.g., Atwater & Stock, 1998; Brink et al., 2000; Dickinson et al., 2009; Nicholson et al., 1994; Saleeby, 2003; Shaw et al., 2015). The transition of the plate boundary from subduction to transform in the Miocene (e.g., Atwater & Stock, 1998) resulted in widespread crustal deformation in the region (Figure 1), involving slab-window magmatism (McCrory et al., 2009), block rotations (Luyendyk, 1991), and tectonic underplating (Saleeby, 2003). Today, the San Andreas Fault (SAF) is commonly treated as the plate boundary between the Pacific and North American plates and accommodates ~75% of their relative motion, whereas the Eastern California Shear Zone (ECSZ) to the east absorbs most

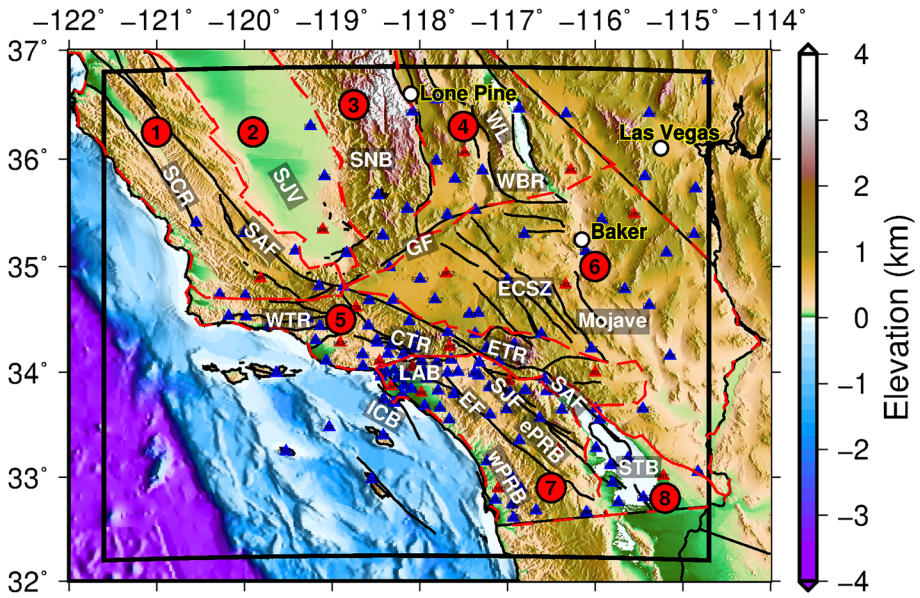

Figure 1. Map of Southern California with topography, bathymetry, and active faults. The solid black rectangle outlines the simulation region. The 148 stations used in this tomographic study are shown as triangles, out of which 19 are selected for line search (shown in red). Faults are indicated by the bold black lines. Labels 1–8 denote the major eight geological provinces with their boundaries delineated by red dash lines: 1. Coastal Ranges; 2. Great Central Valley; 3. Sierra Nevada; 4. Basin and Ranges; 5. Transverse Ranges; 6. Mojave Desert; 7. Peninsular Ranges; 8. Salton Trough. Geological features labeled in bold white letters as referred by subsequent figures: SCR, southern Coast Range; SAF, San Andreas Fault; SJV, San Joaquin Valley; SNB, Sierra Nevada Batholith; GF, Garlock Fault; WL, Walker Lane; WBR, Western Basin and Range; WTR, CTR, and ETR, western, central and eastern Transverse Range; ECSZ, Eastern California Shear Zone; ICB, Inner Continental Borderland; LAB, Los Angeles Basin; EF, Elsinore Fault; SJF, San Joaquin Fault; ePRB and wPRB, east and west Peninsular Ranges Batholith; STB, Salton Trough Basin.

of the remaining deformation (Argus et al., 2011; Savage et al., 1990). In Southern California, the SAF splays into several nearly parallel strike-slip faults, and the deformation along these faults is suggested to occur through localized shearing that likely extends to the upper mantle (Molnar & Dayem, 2010). Geodetic modeling based on elastic block models can explain most of the surface deformation in the region (e.g., Meade & Hager, 2005).

Seismic studies conducted in Southern California provide evidence both for and against the block model. On one hand, distinct crustal velocity contrasts are observed across the SAF (Fang et al., 2018; Hauksson, 2000; Lee et al., 2014; Tape et al., 2009; Wang et al., 2018; Zhao et al., 1996; Zigone et al., 2015), which are accompanied by abrupt changes in the Moho depth (Berg et al., 2018; Qiu et al., 2019; Yan & Clayton, 2007; Zhu & Kanamori, 2000), lithospheric thickness (e.g., Ford et al., 2014), and anisotropic signatures (Barak & Klemperer, 2016; Jiang , Schmandt, & Clayton , 2018). The above lines of evidence are consistent with strong localization of deformation along the SAF. However, this relationship becomes less obvious for other fault systems in the region. In particular, seismogenic zones constrained by seismicity distribution and locking depths based on geodetic data mostly terminate at 15–20 km depths (e.g., Meade & Hager, 2005), making the inference of deformation patterns at depths obscure. Moreover, small-scale mantle dynamics inferred from seismic tomography and numerical modeling (Houseman et al., 2000; Schmandt & Humphreys, 2010; Yang & Forsyth, 2006) might further complicate the crustal deformation by creating different strain regimes at crustal depth, although the real pattern of the deformation may depend on physical parameters that are still poorly constrained. Overall, how plate boundary deformation is accommodated in the deep crust of Southern California remains enigmatic.

Seismic radial anisotropy, defined by the difference between horizontally (V_{SH}) and vertically (V_{SV}) polarized shear wave speed (V_s), provides a unique window to the deformation history of the solid Earth. It allows us to decipher tectonic deformation and flow patterns in the crust and upper mantle (e.g., Luo et al., 2013; Lynner et al., 2018; Shapiro et al., 2004; Xie et al., 2013) through probing the mineral (crystal preferred

orientation, CPO) and structural orientations (shape preferred orientation, SPO) developed from accumulated shear strains (e.g., Karato et al., 2008; Mainprice & Nicolas, 1989). Compared to the abundant isotropic velocity models available for Southern California (e.g., Barak et al., 2015; Hauksson, 2000; Humphreys & Clayton, 1990; Jiang et al., 2018; Schmandt & Humphreys, 2010; Shapiro et al., 2005; Tape et al., 2009; Wang et al., 2018; Yang & Forsyth, 2006), radially anisotropic structures in the region have been less explored and are mostly limited to large-scale studies (Moschetti et al., 2010; Xie et al., 2015). This inhibits detailed interpretation of deformation in Southern California. The purpose of this study is to construct a 3-D radially anisotropic crustal model of Southern California to improve our understanding of deformation mechanisms in the deep crust.

In this study, we use the ambient noise adjoint tomography (ANAT) method developed in our earlier study (Wang et al., 2019) to invert three-component ambient noise data for anisotropic V_S structure in Southern California. The resulting anisotropic model achieves 70% misfit reduction compared to the isotropic model, highlighting the importance of anisotropy in describing seismic properties of the crust in the region. The model reveals new features in the crust which provides valuable insights into understanding deformation mechanisms at the Pacific-North American plate boundary.

2. Data and Method

Our data set consists of transverse-transverse (T-T) and vertical-vertical (Z-Z) component empirical Green's functions (EGFs) at 5–50 s between station pairs extracted by Wang et al. (2019, 2018), which use three-component ambient seismic noise recorded by 148 broadband seismometers in Southern California from January 2006 to December 2012 (Figure 1). The preprocessing of ambient noise data and stacking of the long-term EGFs over 7 years (e.g., Bensen et al., 2007; Yang et al., 2008; Yao et al., 2008) make effective noise sources approximately isotropic (see Figure S1 in the supporting information, for details) and help minimize the phase biases caused by the inhomogeneous source distribution (e.g., Yao & Van Der Hilst, 2009; Wang et al., 2016). Synthetic Green's functions (SGFs) are generated from full-wave numerical simulations in 3-D heterogeneous models based on the spectral-element method (SEM) (e.g., Komatitsch et al., 2004; Komatitsch & Tromp, 1999). We use an irregular finite-element mesh (Wang et al., 2018) that incorporates complex interfaces (i.e., topography, basin depth, and Moho variations) and has a simulation accuracy down to 2 s. Unidirectional (north, east, and vertical) point-force sources with a Gaussian source time function of 1.0 s half duration are placed at the Earth surface to generate three-component synthetics at receivers, which are then rotated to obtain Z-Z component Rayleigh wave and T-T component Love wave SGFs.

The inversion starts with an isotropic model of *M16* (also known as CVM-H6.2), which is derived based on 2–30 s local earthquake waveform data by Tape et al. (2009, 2010) using adjoint tomography. A preconditioned gradient-based optimization method is applied to iteratively improve the model over two stages: (I) isotropic inversion and (II) anisotropic inversion for radial anisotropy. In our previous studies (Stage I), ANAT has been applied to Rayleigh and Love waves separately to obtain the two different isotropic models: $M21R = (\rho_V, V_{PV}, V_{SV})$ from Rayleigh waves (Wang et al., 2018), and $M21L = (\rho_H, V_{PH}, V_{SH})$ from Love waves (Wang et al., 2019). In this study, we perform ANAT to simultaneously minimize the Rayleigh and Love wave traveltime misfit functions between EGFs from ambient noise and SGFs from SEM simulations (see Text S1 for more details) using 3-D sensitivity kernels for multicomponent EGFs calculated based on the adjoint method (Wang et al., 2019). In the anisotropic inversion (Stage II), the two isotropic models (*M21R* and *M21L*) from Stage I are combined to obtain a starting radially anisotropic model $M21 = (\rho, V_{PV}, V_{PH}, V_{SV}, V_{SH}, \eta)$, with an average density parameter $\rho = (\rho_V+\rho_H)/2$ and a dimensionless radially anisotropic parameter ($\eta = 1.0$). In Stage I, we adopt a multiscale strategy to reduce the nonlinearity of the inversion by fitting long period broadband data at 20–50 s first and gradually decrease the shortest period to 10 and 5 s. In the second stage, the EGFs are filtered in four more refined narrow period bands: namely, 6–15, 10–20, 15–30, and 20–40 s, to better image the crustal structures as similarly done in Chen et al. (2014). According to Fichtner (2014), phase traveltimes measured in narrow period bands are less affected by source heterogeneities and data processing schemes compared to waveform-based measurements.

3. Results

3.1. Misfit Reductions

To evaluate the robustness of the inversion, we inspect the model fitting of each iteration by calculating the total misfit as the average of individual traveltime differences between data and synthetics weighted by their uncertainties (Tape et al., 2010; Wang et al., 2018). Figures 2a and 2b show the total traveltime misfit evolutions for Rayleigh and Love waves in the isotropic inversions (from *M16* to *M21R*/*M21L*) and anisotropic inversion (from *M21* to *M28*), respectively. We find that the initial total misfit of Love waves (0.48) is much smaller than that of Rayleigh waves (1.76), meaning the earthquake-based adjoint tomographic model M16 fits the transverse components better than the vertical components. Although the misfits have been reduced largely in the isotropic inversion stage for Rayleigh and Love waves separately, we find that introducing radial anisotropy slightly increases the misfits when we switch from the isotropic models (M21R/M21L) to radially anisotropic model (M21) (Figure S3). This indicates that wave propagation in anisotropic media cannot simply be modeled by two separate simulations based on isotropic models. As the inversion proceeds to anisotropic inversion, the total misfit continues to decrease by about 29.5% for Rayleigh waves (Figure 2a) and 8.6% for Loves (Figure 2b). After seven preconditioned conjugate-gradient iterations, we obtain the final radially anisotropic model *M28*. Note that we use more and narrower period bands in the anisotropic inversion than the previous isotropic inversion, so the total misfit of anisotropic inversion is not necessarily smaller than that of the last iteration in the isotropic case (for Love waves) from a multiscale strategy perspective (Zhu et al., 2015). Compared with the initial isotropic model *M16*, our final model achieves 70% misfit reduction (80% for Rayleigh waves and 33% for Love waves). The mean and standard deviation of overall misfits reduce from 1.04 ± 1.49 to 0.07 ± 0.95 for Rayleigh waves (Figure 2c), and from -0.15 ± 1.21 to -0.02 ± 1.04 for Love waves (Figure 2d).

3.2. Three-Dimensional Shear Wave Anisotropic Model

Selected depth and vertical cross sections of the final model are plotted in Figures 3 and 4 as both Voigt average V_S (defined as $\sqrt{(2V_{SV}^2 + V_{SH}^2)/3}$; e.g., Babuska & Cara, 1991; Zhu et al., 2015), and its radial anisotropy (RA; defined as $(V_{SH} - V_{SV})/V_S$). For the isotropic component (Figures 3a, 3c, and 3e), our model mostly agrees with previous tomographic studies in the region (Figures S14–S22) (Barak et al., 2015; Lee et al., 2014; Tape et al., 2009, 2010). For example, tectonic terranes located west of the SAF show high velocities throughout the crust, corresponding to the magmatic arc systems associated with Laramide subduction in the Mesozoic (Dickinson & Butler, 1998). In contrast, velocities are much lower for the units located east of the SAF. Particularly, pronounced V_S reduction is observed in the midlower crust beneath the Walker Lane, as also seen in Lee et al. (2014) and Jiang, Schmandt, Hansen, et al. (2018). They suggest the low velocity results from active magmatic processes in the crust that are likely linked to mantle dynamics (Boyd et al., 2004; Jones et al., 1994; Zandt et al., 2004). In the following section, we mainly focus on the descriptions of anisotropic features that have not been explored in detail before.

In the shallow crust, most of the study region is characterized by positive anisotropy of moderate amplitude (~4%), including the Mojave region, the ECSZ and most of the Basin and Ranges province (BRP). Particularly strong positive anisotropy is observed beneath the Inner Continental Borderland, the western San Joaquin Valley and southern Coast Ranges (SCR). The rest of the model shows weak or slightly negative anisotropy. Of note is that the SAF and Garlock faults are observed as boundaries delineating distinct contrasts in velocity and anisotropy.

In the middle/lower crust, the most pronounced feature is that the southwestern side of the SAF displays strong negative radial anisotropy, with amplitudes up to ~8%. Horizontally, the zone of negative anisotropy is bounded by the Pacific coast to the west and the SAF to the east, extending continuously from the western Transverse Ranges (WTR), cutting across the central Transverse Ranges (CTR), and further south to the entire Peninsular Ranges. Vertically, its upper boundary approximately starts at 15 km depth with slight topography variations along the geological units (e.g., D-D′ in Figure 4), while the lower boundary seems to be terminated by the Moho. The ECSZ shows moderate negative anisotropy at the same depth range, as a transition to the positive anisotropy feature in the broad area of BRP to the east.

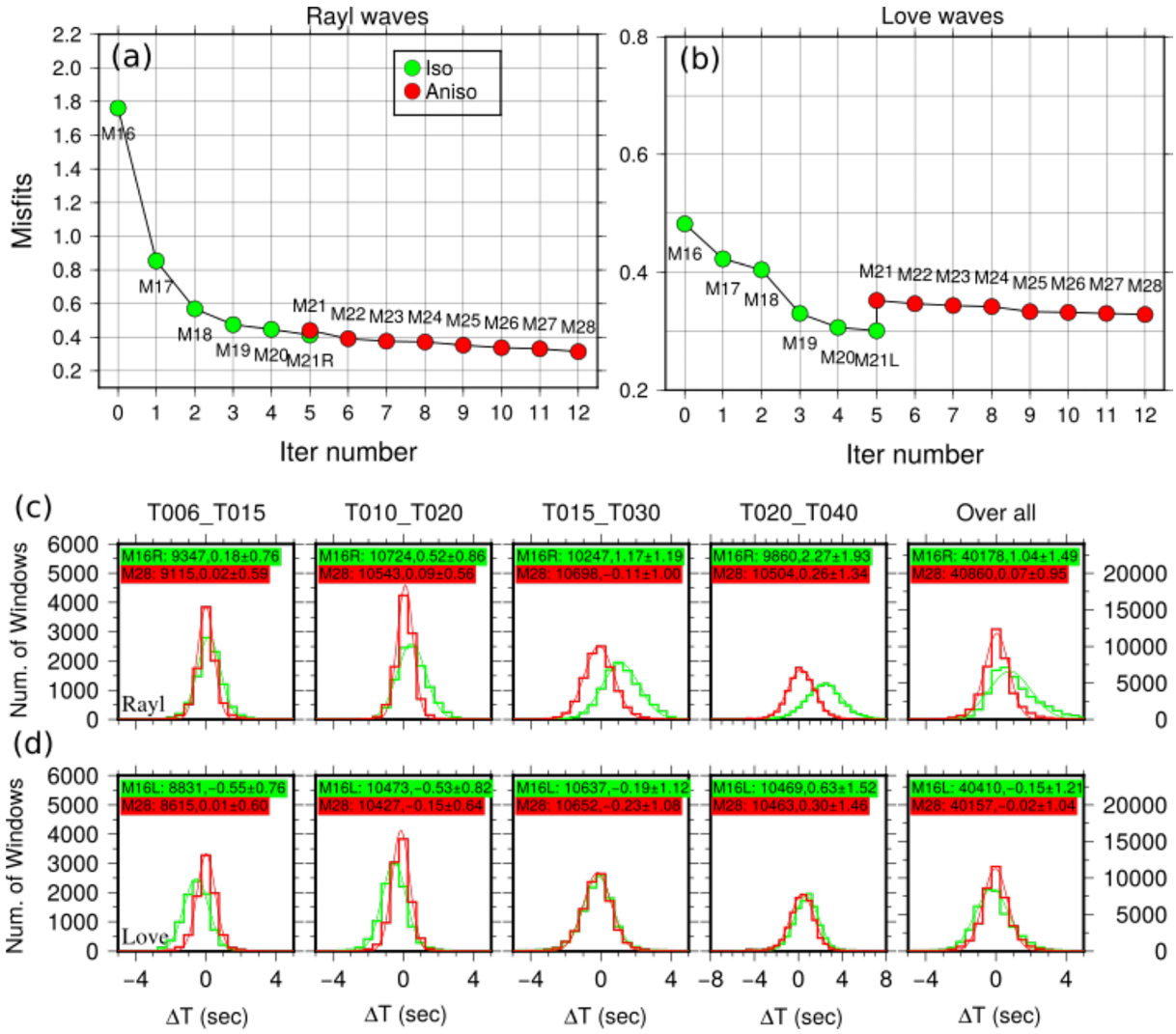

Figure 2. (a and b) The total traveltime misfit evolution over iterations for measurements between EGFs and SGFs made from Z-Z component Rayleigh waves and T-T component Love waves, respectively. The green solid circles are from isotropic inversions based on Rayleigh wave ANAT (Wang et al., 2018) and Love wave ANAT (Wang et al., 2019), and the red solid circles are from anisotropic inversion in this study. Note the total misfits of Rayleigh and Love waves increase a little for model *M21* relative to the isotropic models (*M21R*/*M21L*) with more period bands data used and the introduction of radial anisotropy. (c and d) The differential traveltime histograms of different models for Rayleigh and Love waves, respectively. The green bars represent the traveltime histograms for the initial isotropic model *M16* and the red bars are the corresponding traveltime histograms for our final anisotropic model *M28*. The histograms are measured at four narrow period bands plotted in different columns, and the overall histograms are presented in the last column. The number of measurements, average value, and standard deviations are also shown in colored text boxes.

In the uppermost mantle (Figure 3f), our model shows positive radial anisotropy across the entire region. The distribution of anisotropy correlates well with the isotropic velocity model, with localized concentrations beneath the Sierra Nevada Batholith, western BRP, CTR, and Los Angeles Basin.

4. Discussions

4.1. Inversion Assessment

We conduct a resolution test to demonstrate that our inversion can resolve small-scale perturbations and distinguish the velocity difference between V_{SV} and V_{SH}, thus the radial anisotropy (See Text S3). To validate our anisotropic model, we conduct forward simulations for 143 local earthquakes that are used in Tape et al. (2010) but not included in our inversion, and then compare the observed waveforms with the synthetics predicted from *M16* and *M28* (see Texts S4–5 for more details). Wang et al. (2018) validated the V_{SV} model

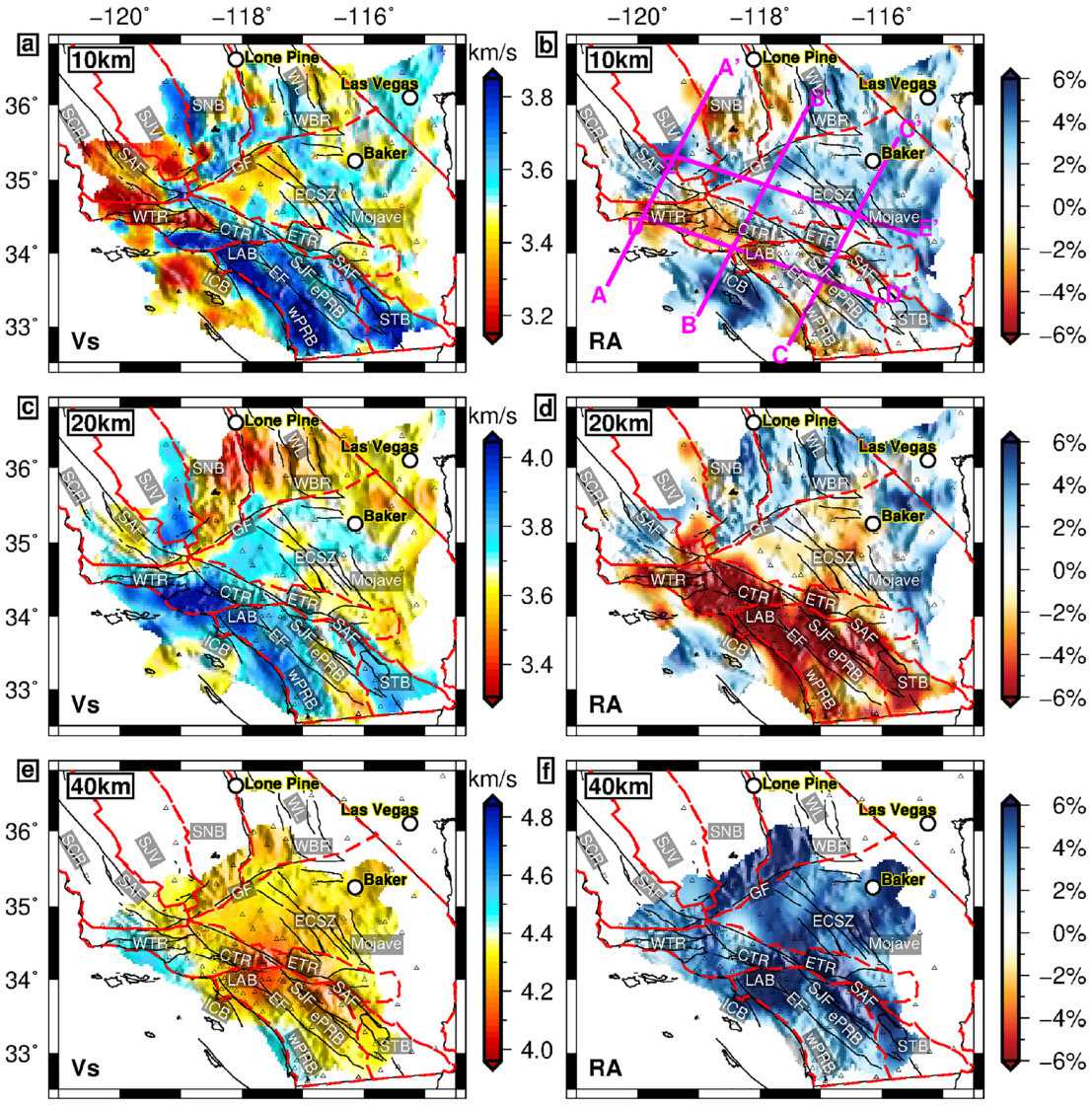

Figure 3. Horizontal cross sections of Voigt-averaged shear wave velocity (V_s) and radial anisotropy (RA) at depths of 10 km (a, b), 20 km (c, d), and 40 km (e, f). Locations of the profiles (AA′-EE′) in Figure 4 are plotted as magenta solid lines in (b).

M21R by comparing *M16* using the same 143 earthquake data and found that misfits are significantly reduced in the intermediate period band (10–30 s) for vertical components but increase a little for transverse components. This is reasonable because only Rayleigh waves are used to construct the model *M21R*, and we expect the introduction of radial anisotropy helps to improve data fitting for transverse components. Indeed, the final anisotropic model *M28* from this study shows large misfit reductions compared to the isotropic model *M16* for all the three components in the targeted period band (10–30 s) (Figure S6), which confirms that crustal radial anisotropy is significant in Southern California.

4.2. Origin of Seismic Radial Anisotropy

The broadly distributed positive anisotropy in the crust beneath the BRP and the uppermost mantle across the entire region is generally consistent with the anisotropic models of Moschetti et al. (2010) and Xie et al. (2015). In particular, both studies found that the region of positive anisotropy coincides with geological areas experiencing significant extension through the Cenozoic (Wernicke, 1992). They further attribute this anisotropic feature to subhorizontal alignment of foliation planes of mica and amphibole in the crust and olivine in the upper mantle developed during the strongly extensional deformation regime. Fast velocities

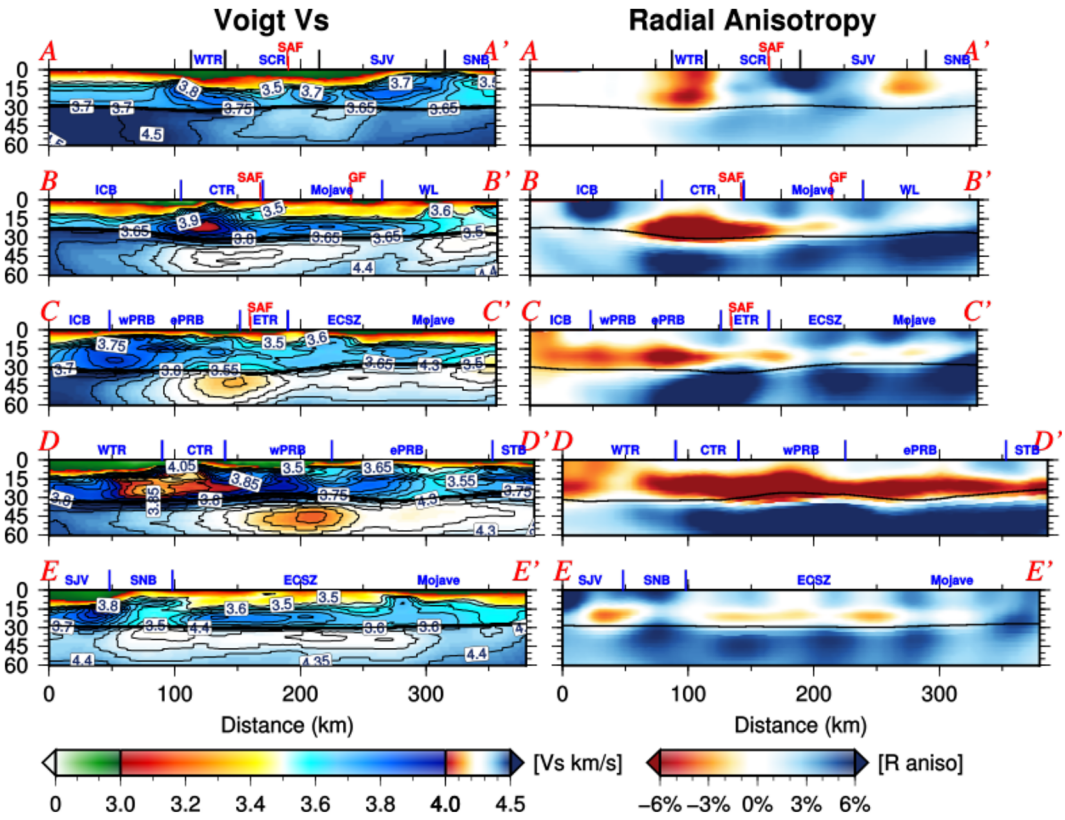

Figure 4. Voigt V_S (left panels) and radial anisotropy (right panels) along the profiles shown in Figure 3b. Geological features (with abbreviations shown in Figure 1) are marked by blue lines and bold texts; the depths of Moho (Zhu et al., 2000) are plotted in black solid lines. Major faults (SAF: San Andreas Fault; GF: Garlock Fault) are marked by red dashed lines and bold text.

and thinned crust in these positive radial anisotropic zones (Hauksson, 2000; Lekic et al., 2011; Yang & Forsyth, 2006) support this idea, with which we generally agree. However, the negative anisotropy in the middle/lower crust west of the SAF has not been observed before. We focus on the discussion of its origin and geological implications throughout the rest of this section.

The origin of the negative anisotropy is intriguing, as it is rarely observed at middle/lower crustal depths in previous anisotropic tomography studies (e.g., Luo et al., 2013; Wilgus et al., 2020; Xie et al., 2013). For example, a large-scale model covering the western United States (Xie et al., 2015) only exhibits small patches of negative anisotropy in the front of the Cascadia arc, with underlying mechanisms remaining to be explored. Negative anisotropy is observed more often in volcanic settings where active melt lenses might be injected into the crust as dikes, such as at Piton de la Fournaise (Mordret et al., 2015) and the Altiplano-Puna Volcanic Complex in the central Andes (Lynner et al., 2018). The broad sensitivity of intermediate period surface waves (e.g., 15–30 s) at depths of middle/lower crust indicates such melts would have to be present in substantial amounts to be detected (e.g., Jiang, Schmandt, Farrell, et al., 2018). The slab-window magmatism in the Cenozoic may have generated a large pulse of a thermal anomaly along the California coast (McCrory et al., 2009) and thus potentially lead to the formation of strong SPO of active melts in the region. However, both the distinction of anisotropic signatures between the WTR and SCR and the very high velocity (>3.8 km/s) in the middle/lower crust observed in this study contrast with this hypothesis in which spatially continuous low velocity anomalies would have been generated. Moreover, the V_S structure indicates <1% of melt is present in the uppermost mantle today (Schmandt & Humphreys, 2010; Yang & Forsyth, 2006), making SPO from active dike injections less likely.

Previous studies mostly tend to attribute middle-lower crustal anisotropy to the CPO of mica and amphibole, which is approximated to have hexagonal symmetry with a slow axis (Ko & Jung, 2015; Lloyd et al., 2009; Tatham et al., 2008). To explain the negative anisotropy observed in this study, the mica- and

amphibole-bearing rocks have to show subvertical foliation. The extensive fault zones in Southern California might provide mechanical condition for the development of subvertical dominant foliation in the lower crust, but it is difficult to reconcile its distribution over a broad region. Through harmonic analysis of receiver functions, Porter et al. (2011) and Ozacar and Zandt (2009) identified a lower-crust anisotropic layer with dipping foliation beneath the broad area of Southern California and near Parkfield. They interpret the dipping feature to be fossilized fabrics of schists developed in a basal crustal shear zone related to Laramide flat slab subduction (McQuarrie & Wernicke, 2005; Saleeby, 2003). We find the upper boundary of our anisotropic feature (B-B′ in Figure 4) generally agrees with the top of the anisotropic layer from receiver functions, which further aligns with the "bright" reflectors identified in the active LARSE experiment (Fuis et al., 2001, 2007; Porter et al., 2011; Ryberg & Fuis, 1998). However, laboratory measurements on the exposed schists indicate relatively lower velocities (<3.7 km/s) (Godfrey et al., 2000; Pellerin & Christensen, 1998) compared to our observations (>3.8 km/s). One possible explanation for this discrepancy is that these samples represent the felsic compositional end of the schists considering their shallow exposure depth, and they might become more mafic with depth (Rudnick & Fountain, 1995). Indeed, anisotropic modeling based on lab-measured elastic tensors of Pelona schists (e.g., Graham & Powell, 1984) indicates that comparable isotropic and anisotropic features to our observation can be generated with schists in relatively more mafic composition (e.g., 66% amphibole, 24% plagioclase, 7% biotite and ~2% garnet) (Sarah J Brownlee et al., personal communication, 8 April, 2020).

Steeply dipping amphibole schists may be a potential candidate for our observed anisotropy feature as discussed above. However, it remains enigmatic how a regional, and presumably extensive tectonic event leads to deformation fabrics terminated right at the present SAF. In this study, we propose an alternative mechanism, that the negative anisotropy could be a result of subhorizontal alignment of the slow velocity plane of plagioclase. Plagioclase is one of the dominant minerals in the crust (Christensen, 1996), particularly in mafic rocks (Almqvist & Mainprice, 2017), though its CPO has received much less attention compared to mica and amphibole for the interpretation of crustal anisotropy. However, recent studies indicate it may contribute more significantly to anisotropic signatures than previously thought (Almqvist & Mainprice, 2017; Bernard & Behr, 2017). Compared to mica and amphibole that display hexagonal symmetry with a slow axis (note this differs from the concept of a vertical/horizontal symmetry axis) (Lloyd et al., 2009; Tatham et al., 2008), plagioclase is demonstrated to exhibit strong anisotropy that approximates hexagonal symmetry with a fast axis (Brownlee et al., 2017). Another distinctive feature of plagioclase is that its fast axis tends to align perpendicular to the shear plane and foliation plane, in contrast to, for example, olivine, where the fast axis aligns parallel to shear (Bernard & Behr, 2017). If plagioclase fabric is dominant, the negative anisotropy observed in Southern California may be caused by subhorizontal foliation in plagioclase-rich deformed rock, which would have vertical fast axis orientations (Bernard & Behr, 2017). The origin of the subhorizontal foliation could stem from subhorizontal shear during flat-slab subduction, from previous extensional episodes, or maybe relict magmatic fabric (Bernard & Behr, 2017) developed earlier during emplacement of the plutons. Although the deformation mechanism for the development of plagioclase CPO is still not fully understood, a recent analysis of xenoliths sampling the lower crust of the adjacent Mojave region found strong CPO in plagioclase (Bernard & Behr, 2017). As emphasized by Bernard and Behr (2017), a change in seismic anisotropy with depth may reflect a change in mineralogy with depth rather than a change in deformation regime. We think this could be the case in Southern California. Interestingly, the negative anisotropy in our model is weak beneath the Mojave region, and this could be caused by Cenozoic deformation disrupting the middle-lower crust as indicated by the local Moho topography (Yan & Clayton, 2007).

4.3. Implications for Crustal Deformation

The distinction between the two mechanisms discussed above requires additional observational constraints, such as azimuthal anisotropy, or through a joint inversion of azimuthal and radial anisotropy for the oriented elastic tensor (e.g., Xie et al., 2015) and is therefore beyond the scope of this study. However, the new mechanism of plagioclase CPO to explain the negative anisotropy feature has broad implications for understanding crustal deformation. First, it highlights the potential large contribution of plagioclase to anisotropic signatures observed in the crust. Second, even though the middle/lower crust is characterized by negative radial anisotropy, which is different from the positive radial anisotropy in the upper crust and uppermost mantle, it does not necessarily mean the middle/lower crust is decoupled,

as the foliation planes of plagioclase are still subhorizontally aligned except that its fast-velocity axes are vertical. Third, the distinct contrast of the anisotropy across the SAF is consistent with the SAF being a plate boundary that at least cuts through the crust. Another possibility is that regions with negative radial anisotropy played a role in localization of the SAF during its development due to rheological differences from lithological variations.

We note another anisotropic feature in our model, namely, that the strength of the anisotropy does not seem to decrease when moving away from the SAF shear zone. This might suggest the shear deformation along the SAF system is unlikely to be the major factor contributing to the negative anisotropy, or at least it is not localized near the SAF. On the other hand, receiver function studies in the region (Porter et al., 2011; Schulte-Pelkum & Mahan, 2014) show most stations close to faults indicate fault-parallel foliation. Seismic and structural analysis on the SAF, San Jacinto Fault, and Elsinore Faults suggests dipping fault geometries (Barak et al., 2015; Dorsey et al., 2012; Fuis et al., 2007, 2012; Mason et al., 2017; Ross et al., 2017; White et al., 2019) and extensional structures can be reactivated as dipping strike-slip, generating dipping fast planes with fault-parallel strikes picked up by receiver functions. Therefore, our anisotropy model is still consistent with the azimuthal anisotropic features from receiver functions (Audet, 2015; Ozacar & Zandt, 2009; Schulte-Pelkum & Mahan, 2014). This highlights the juxtaposition of both currently localized deformation accommodating boundary dynamics along deep-rooted faults as well as broader deformation in the middle/lower crust due to past regional deformation in Southern California.

5. Conclusions

In this study, we apply ambient noise adjoint tomography to three-component ambient noise data in Southern California to construct a new radially anisotropic shear wave velocity model. A multiscale strategy is adopted to improve the isotropic V_{SV} and V_{SH} models by fitting empirical Green's functions with synthetics at four narrow period bands between 6–40 s. The total misfit is reduced by 70% and converged within a total of 13 conjugation-gradient iterations. The final anisotropic model reveals broadly distributed positive anisotropy (+4%) in the crust across the BRP, which is consistent with the interpretation of CPO of mica/amphibole from significant crustal extension accumulated in the Cenozoic Era as suggested by previous studies. An oblique zone of negative radial anisotropy (−6%) bounded by the Pacific coast and SAF is observed in the middle/lower crust and is attributed to steeply dipping of schists as suggested by previous studies but probably with more mafic composition (e.g., amphibole and garnet). Alternatively, it can be formed by the subhorizontal alignment of plagioclase, as newly observed in laboratory experiments on xenoliths from the region. In particular, this latter new mechanism highlights the potentially complex CPO patterns resulting from different lithospheric mineralogy with the same strain regime.

Data Availability Statement

The seismic data used were downloaded from the Caltech/USGS Southern California Seismic Network (https://doi.org/10.7914/SN/CI) and IRIS Transportable Array (https://doi.org/10.7914/SN/TA). Our final model is available at IRIS EMC (http://ds.iris.edu/ds/products/emc-socalanat_vsrawang2020).

Acknowledgments

The authors would like to thank the developers of the open-source software *SPECFEM3D* for their continued community work; Brandon Schmandt, John Shaw, Sarah Brownlee, and Andreas Plesch for fruitful discussions; Sarah Brownlee for modeling of elastic tensors for relevant lithologies; Editor Lucy Flesch, Hejun Zhu, and another anonymous reviewer for comments that helped improve the manuscript significantly. K. Wang and Q. Liu are supported by the NSERC Discovery Grant 487237. Computations for this study were performed on hardware acquired through the combined funding of Canada Foundation for Innovation (CFI), Ontario Research Fund (ORF), and University of Toronto Startup Fund and partly hosted by the SciNet HPC Consortium. Y. Yang is supported by Australian Research Council Future Fellowship (FT130101220) and Discovery Project (DP190102940). Schulte-Pelkum's contribution was supported by NSF Grants EAR-1251193, 1735890, and 1927246, and SCEC Grant 17097. This is contribution 1509 from the ARC Centre of Excellence for Core to Crust Fluid Systems (http://www.ccfs.mq.edu.au) and 1393 in the GEMOC Key Centre (http://www.gemoc.mq.edu.au).

References

Almqvist, B. S., & Mainprice, D. (2017). Seismic properties and anisotropy of the continental crust: Predictions based on mineral texture and rock microstructure. *Reviews of Geophysics*, *55*, 367–433. https://doi.org/10.1002/2016RG000552

Argus, D. F., Gordon, R. G., & DeMets, C. (2011). Geologically current motion of 56 plates relative to the no-net-rotation reference frame. *Geochemistry, Geophysics, Geosystems*, *12*, Q11001. https://doi.org/10.1029/2011GC003751

Atwater, T., & Stock, J. (1998). Pacific-North America plate tectonics of the Neogene southwestern United States: An update. *International Geology Review*, *40*(5), 375–402. https://doi.org/10.1080/00206819809465216

Audet, P. (2015). Layered crustal anisotropy around the San Andreas Fault near Parkfield, California. *Journal of Geophysical Research: Solid Earth*, *120*, 3527–3543. https://doi.org/10.1002/2014JB011821

Babuska, V., & Cara, M. (1991). *Seismic Anisotropy in the Earth*. Dordrecht: KluwerAcad. https://doi.org/10.1007/978-94-011-3600-6

Barak, S., & Klemperer, S. L. (2016). Rapid variation in upper-mantle rheology across the San Andreas fault system and Salton Trough, southernmost California, USA. *Geology*, *44*(77), 575–578. https://doi.org/10.1130/G37847.1

Barak, S., Klemperer, S. L., & Lawrence, J. F. (2015). San Andreas Fault dip, Peninsular Ranges mafic lower crust and partial melt in the Salton Trough, Southern California, from ambient-noise tomography. *Geochemistry, Geophysics, Geosystems*, *16*, 3946–3972. https://doi.org/10.1002/2015GC005970

Bensen, G. D., Ritzwoller, M. H., Barmin, M. P., Levshin, A. L., Lin, F., Moschetti, M. P., et al. (2007). Processing seismic ambient noise data to obtain reliable broad-band surface wave dispersion measurements. *Geophysical Journal International*, *169*(3), 1239–1260. https://doi.org/10.1111/j.1365-246X.2007.03374.x

Berg, E. M., Lin, F.-C., Allam, A., Qiu, H., Shen, W., & Ben-Zion, Y. (2018). Tomography of Southern California via bayesian joint inversion of rayleigh wave ellipticity and phase velocity from ambient noise cross-correlations. *Journal of Geophysical Research: Solid Earth*, *123*(11), 9933–9949. https://doi.org/10.1029/2018jb016269

Bernard, R. E., & Behr, W. M. (2017). Fabric heterogeneity in the Mojave lower crust and lithospheric mantle in Southern California. *Journal of Geophysical Research: Solid Earth*, *122*, 5000–5025. https://doi.org/10.1002/2017JB014280

Boyd, O. S., Jones, C. H., & Sheehan, A. F. (2004). Foundering lithosphere imaged beneath the southern Sierra Nevada, California, USA. *Science*, *305*(5684), 660–662. https://doi.org/10.1126/science.1099181

Brink, U. S. T., Zhang, J., Brocher, T. M., Okaya, D. A., Klitgord, K. D., & Fuis, G. S. (2000). Geophysical evidence for the evolution of the California Inner Continental Borderland as a metamorphic core complex. *Journal of Geophysical Research*, *105*(B3), 5835–5857. https://doi.org/10.1029/1999JB900318

Brownlee, S. J., Schulte-Pelkum, V., Raju, A., Mahan, K., Condit, C., & Orlandini, O. F. (2017). Characteristics of deep crustal seismic anisotropy from a compilation of rock elasticity tensors and their expression in receiver functions. *Tectonics*, *36*, 1835–1857. https://doi.org/10.1002/2017TC004625

Burchfiel, B., & Davis, G. A. (1972). Structural framework and evolution of the southern part of the cordilleran Orogen, Western United States. *American Journal of Science*, *272*(2), 97–118. https://doi.org/10.2475/ajs.272.2.97

Chen, M., Huang, H., Yao, H., Hilst, R., & Niu, F. (2014). Low wave speed zones in the crust beneath SE Tibet revealed by ambient noise adjoint tomography. *Geophysical Research Letters*, *41*, 334–340. https://doi.org/10.1002/2013GL058476

Christensen, N. I. (1996). Poisson's ratio and crustal seismology. *Journal of Geophysical Research*, *101*(B2), 3139–3156. https://doi.org/10.1029/95jb03446

Dickinson, W. R., & Butler, R. F. (1998). Coastal and Baja California paleomagnetism reconsidered. *Geological Society of America Bulletin*, *110*(10), 1268–1280. https://doi.org/10.1130/0016-7606(1998)110%31268:CABCPR%3E2.3.CO;2

Dickinson, W. R., Kay, S., & Ramos, V. (2009). Anatomy and global context of the North American Cordillera, Backbone of the Americas: Shallow subduction, plateau uplift, and ridge and terrane collision. *Geological Society of America Memoirs*, *204*, 1–29.

Dorsey, R. J., Axen, G. J., Peryam, T. C., & Kairouz, M. E. (2012). Initiation of the Southern Elsinore Fault at ~1.2 Ma: Evidence from the Fish Creek-Vallecito Basin, Southern California. *Tectonics*, *31*, TC2006. https://doi.org/10.1029/2011tc003009

Fang, H., Yao, H., Zhang, H., Thurber, C., Ben-Zion, Y., & van der Hilst, R. D. (2018). Vp/Vs tomography in the Southern California plate boundary region using body and surface wave traveltime data. *Geophysical Journal International*, *216*(1), 609–620. https://doi.org/10.1093/gji/ggy458

Fichtner, A. (2014). Source and processing effects on noise correlations. *Geophysical Journal International*, *197*(3), 1527–1531. https://doi.org/10.1093/gji/ggu093

Ford, H. A., Fischer, K. M., & Lekic, V. (2014). Localized shear in the deep lithosphere beneath the San Andreas Fault System. *Geology*, *42*(4), 295–298. https://doi.org/10.1130/G35128.1

Fuis, G., Ryberg, T., Godfrey, N., Okaya, D., & Murphy, J. (2001). Crustal structure and tectonics from the Los Angeles basin to the Mojave Desert, Southern California. *Geology*, *29*(1), 15–18. https://doi.org/10.1130/0091-7613(2001)029%30015:CSATFT%3E2.0.CO;2

Fuis, G. S., Kohler, M. D., Scherwath, M., ten Brink, U., Avendonk, H. J. A. V., & Murphy, J. M. (2007). A comparison between the transpressional plate boundaries of South Island, New Zealand, and Southern California, USA: The Alpine and San Andreas Fault systems. In *A continental plate boundary: Tectonics at South Island, New Zealand* (pp. 307–327). Washington, DC: American Geophysical Union. https://doi.org/10.1029/175gm16

Fuis, G. S., Scheirer, D. S., Langenheim, V. E., & Kohler, M. D. (2012). A new perspective on the geometry of the San Andreas Fault in Southern California and its relationship to lithospheric structure. *Bulletin of the Seismological Society of America*, *102*(1), 236–251. https://doi.org/10.1785/0120110041

Godfrey, N. J., Christensen, N. I., & Okaya, D. A. (2000). Anisotropy of schists: Contribution of crustal anisotropy to active source seismic experiments and shear wave splitting observations. *Journal of Geophysical Research*, *105*(B12), 27,991–28,007. https://doi.org/10.1029/2000JB900286

Graham, C. M., & Powell, R. (1984). A garnet–hornblende geothermometer: Calibration, testing, and application to the Pelona schist, Southern California. *Journal of Metamorphic Geology*, *2*(1), 13–31. https://doi.org/10.1111/j.1525-1314.1984.tb00282.x

Hauksson, E. (2000). Crustal structure and seismicity distribution adjacent to the Pacific and North America plate boundary in Southern California. *Journal of Geophysical Research*, *105*(B6), 13,875–13,903. https://doi.org/10.1029/2000JB900016

Houseman, G. A., Neil, E. A., & Kohler, M. D. (2000). Lithospheric instability beneath the transverse ranges of California. *Journal of Geophysical Research*, *105*(B7), 16,237–16,250. https://doi.org/10.1029/2000JB900118

Humphreys, E. D., & Clayton, R. W. (1990). Tomographic image of the Southern California mantle. *Journal of Geophysical Research*, *95*(B12), 19,725–19,746. https://doi.org/10.1029/JB095iB12p19725

Jiang, C., Schmandt, B., & Clayton, R. W. (2018). An anisotropic contrast in the lithosphere across the central San Andreas fault. *Geophysical Research Letters*, *45*, 3967–3975. https://doi.org/10.1029/2018GL077476

Jiang, C., Schmandt, B., Farrell, J., Lin, F.-C., & Ward, K. M. (2018). Seismically anisotropic magma reservoirs underlying silicic calderas. *Geology*, *46*(8), 727–730. https://doi.org/10.1130/G45104.1

Jiang, C., Schmandt, B., Hansen, S. M., Dougherty, S. L., Clayton, R. W., Farrell, J., & Lin, F.-C. (2018). Rayleigh and S wave tomography constraints on subduction termination and lithospheric foundering in central California. *Earth and Planetary Science Letters*, *488*, 14–26. https://doi.org/10.1016/j.epsl.2018.02.009

Jones, C. H., Kanamori, H., & Roecker, S. W. (1994). Missing roots and mantle "drips": Regional Pn and teleseismic arrival times in the southern Sierra Nevada and vicinity, California. *Journal of Geophysical Research*, *99*(B3), 4567–4601. https://doi.org/10.1029/93JB01232

Karato, S.-I., Jung, H., Katayama, I., & Skemer, P. (2008). Geodynamic significance of seismic anisotropy of the upper mantle: New insights from laboratory studies. *Annual Review of Earth and Planetary Sciences*, *36*(1), 59–95. https://doi.org/10.1146/annurev.earth.36.031207.124120

Ko, B., & Jung, H. (2015). Crystal preferred orientation of an amphibole experimentally deformed by simple shear. *Nature Communications*, *6*(1), 6586. https://doi.org/10.1038/ncomms7586

Komatitsch, D., Liu, Q., Tromp, J., Suss, P., Stidham, C., & Shaw, J. H. (2004). Simulations of ground motion in the Los Angeles basin based upon the spectral-element method. *Bulletin of the Seismological Society of America*, *94*(1), 187–206. https://doi.org/10.1785/0120030077

Komatitsch, D., & Tromp, J. (1999). Introduction to the spectral element method for three-dimensional seismic wave propagation. *Geophysical Journal International*, *139*(3), 806–822. https://doi.org/10.1046/j.1365-246x.1999.00967.x

Lee, E.-J., Chen, P., Jordan, T. H., Maechling, P. B., Denolle, M. A., & Beroza, G. C. (2014). Full-3-D tomography for crustal structure in Southern California based on the scattering-integral and the adjoint-wavefield methods. *Journal of Geophysical Research: Solid Earth*, *119*, 6421–6451. https://doi.org/10.1002/2014JB011346

Lekic, V., French, S. W., & Fischer, K. M. (2011). Lithospheric thinning beneath rifted regions of Southern California. *Science*, *334*(6057), 783–787. https://doi.org/10.1126/science.1208898

Lloyd, G. E., Butler, R. W., Casey, M., & Mainprice, D. (2009). Mica, deformation fabrics and the seismic properties of the continental crust. *Earth and Planetary Science Letters*, *288*(1–2), 320–328. https://doi.org/10.1016/j.epsl.2009.09.035

Luo, Y., Xu, Y., & Yang, Y. (2013). Crustal radial anisotropy beneath the Dabie orogenic belt from ambient noise tomography. *Geophysical Journal International*, *195*(2), 1149–1164. https://doi.org/10.1093/gji/ggt281

Luyendyk, B. P. (1991). A model for Neogene crustal rotations, transtension, and transpression in Southern California. *Geological Society of America Bulletin*, *103*(11), 1528–1536. https://doi.org/10.1130/0016-7606(1991)103%31528:AMFNCR%3E2.3.CO;2

Lynner, C., Beck, S. L., Zandt, G., Porritt, R. W., Lin, F.-C., & Eilon, Z. C. (2018). Midcrustal deformation in the Central Andes constrained by radial anisotropy. *Journal of Geophysical Research: Solid Earth*, *123*, 4798–4813. https://doi.org/10.1029/2017JB014936

Mainprice, D., & Nicolas, A. (1989). Development of shape and lattice preferred orientations: Application to the seismic anisotropy of the lower crust. *Journal of Structural Geology*, *11*(1–2), 175–189. https://doi.org/10.1016/0191-8141(89)90042-4

Mason, C. C., Spotila, J. A., Axen, G., Dorsey, R. J., Luther, A., & Stockli, D. F. (2017). Two-phase exhumation of the Santa Rosa Mountains: Low- and high-angle Normal faulting during initiation and evolution of the southern San Andreas Fault System. *Tectonics*, *36*, 2863–2881. https://doi.org/10.1002/2017TC004498

McCrory, P. A., Wilson, D. S., & Stanley, R. G. (2009). Continuing evolution of the Pacific-Juan de Fuca-North America slab window system—A trench-ridge-transform example from the Pacific rim. *Tectonophysics*, *464*(1–4), 30–42. https://doi.org/10.1016/j.tecto.2008.01.018

McQuarrie, N., & Wernicke, B. P. (2005). An animated tectonic reconstruction of south-western North America since 36 Ma. *Geosphere*, *1*(3), 147–172. https://doi.org/10.1130/GES00016.1

Meade, B. J., & Hager, B. H. (2005). Spatial localization of moment deficits in Southern California. *Journal of Geophysical Research*, *110*, B04402. https://doi.org/10.1029/2004JB003331

Molnar, P., & Dayem, K. E. (2010). Major intracontinental strike-slip faults and contrasts in lithospheric strength. *Geosphere*, *6*(4), 444–467. https://doi.org/10.1130/GES00519.1

Mordret, A., Rivet, D., Landès, M., & Shapiro, N. M. (2015). Three-dimensional shear velocity anisotropic model of Piton de la Fournaise volcano (La Réunion Island) from ambient seismic noise. *Journal of Geophysical Research: Solid Earth*, *120*, 406–427. https://doi.org/10.1002/2014JB011654

Moschetti, M., Ritzwoller, M., Lin, F., & Yang, Y. (2010). Seismic evidence for widespread western-US deep-crustal deformation caused by extension. *Nature*, *464*(7290), 885–889. https://doi.org/10.1038/nature08951

Nicholson, C., Sorlien, C. C., Atwater, T., Crowell, J. C., & Luyendyk, B. P. (1994). Microplate capture, rotation of the western Transverse Ranges, and initiation of the San Andreas transform as a low-angle fault system. *Geology*, *22*(6), 491–495. https://doi.org/10.1130/0091-7613(1994)022%30491:MCROTW%3E2.3.CO;2

Ozacar, A. A., & Zandt, G. (2009). Crustal structure and seismic anisotropy near the San Andreas Fault at Parkfield, California. *Geophysical Journal International*, *178*(2), 1098–1104. https://doi.org/10.1111/j.1365-246X.2009.04198.x

Pellerin, C. L. M., & Christensen, N. I. (1998). Interpretation of crustal seismic velocities in the San Gabriel-Mojave region, Southern California. *Tectonophysics*, *286*(1–4), 253–271. https://doi.org/10.1016/S0040-1951(97)00269-2

Porter, R., Zandt, G., & McQuarrie, N. (2011). Pervasive lower-crustal seismic anisotropy in Southern California: Evidence for underplated schists and active tectonics. *Lithosphere*, *3*(3), 201–220. https://doi.org/10.1130/L126.1

Qiu, H., Lin, F.-C., & Ben-Zion, Y. (2019). Eikonal tomography of the Southern California plate boundary region. *Journal of Geophysical Research: Solid Earth*, *124*(9), 9755–9779. https://doi.org/10.1029/2019JB017806

Ross, Z. E., Hauksson, E., & Ben-Zion, Y. (2017). Abundant off-fault seismicity and orthogonal structures in the San Jacinto fault zone. *Science Advances*, *3*(3), e1601946. https://doi.org/10.1126/sciadv.1601946

Rudnick, R. L., & Fountain, D. M. (1995). Nature and composition of the continental crust: A lower crustal perspective. *Reviews of Geophysics*, *33*(3), 267–309. https://doi.org/10.1029/95RG01302

Ryberg, T., & Fuis, G. S. (1998). The San Gabriel Mountains bright reflective zone: Possible evidence of young mid-crustal thrust faulting in Southern California. *Tectonophysics*, *286*(1–4), 31–46. https://doi.org/10.1016/S0040-1951(97)00253-9

Saleeby, J. (2003). Segmentation of the Laramide slab—Evidence from the southern Sierra Nevada region. *Geological Society of America Bulletin*, *115*(6), 655–668. https://doi.org/10.1130/0016-7606(2003)115%30655:SOTLSF%3E2.0.CO;2

Savage, J. C., Lisowski, M., & Prescott, W. H. (1990). An apparent shear zone trending north-northwest across the Mojave Desert into Owens Valley, eastern California. *Geophysical Research Letters*, *17*(12), 2113–2116.

Schmandt, B., & Humphreys, E. (2010). Seismic heterogeneity and small-scale convection in the Southern California upper mantle. *Geochemistry, Geophysics, Geosystems*, *11*, Q05004. https://doi.org/10.1029/2010GC003042

Schulte-Pelkum, V., & Mahan, K. H. (2014). A method for mapping crustal deformation and anisotropy with receiver functions and first results from USArray. *Earth and Planetary Science Letters*, *402*, 221–233. https://doi.org/10.1016/j.epsl.2014.01.050

Shapiro, N. M., Campillo, M., Stehly, L., & Ritzwoller, M. H. (2005). High-resolution surface-wave tomography from ambient seismic noise. *Science*, *307*(5715), 1615–1618. https://doi.org/10.1126/science.1108339

Shapiro, N. M., Ritzwoller, M. H., Molnar, P., & Levin, V. (2004). Thinning and flow of Tibetan crust constrained by seismic anisotropy. *Science*, *305*(5681), 233–236. https://doi.org/10.1126/science.1098276

Shaw, J. H., Plesch, A., Tape, C., Suess, M. P., Jordan, T. H., Ely, G., et al. (2015). Unified structural representation of the Southern California crust and upper mantle. *Earth and Planetary Science Letters*, *415*, 1–15. https://doi.org/10.1016/j.epsl.2015.01.016

Tape, C., Liu, Q., Maggi, A., & Tromp, J. (2009). Adjoint tomography of the Southern California crust. *Science*, *325*(5943), 988–992. https://doi.org/10.1126/science.1175298

Tape, C., Liu, Q., Maggi, A., & Tromp, J. (2010). Seismic tomography of the Southern California crust based on spectral-element and adjoint methods. *Geophysical Journal International*, *180*(1), 433–462. https://doi.org/10.1111/j.1365-246X.2009.04429.x

Tatham, D., Lloyd, G., Butler, R., & Casey, M. (2008). Amphibole and lower crustal seismic properties. *Earth and Planetary Science Letters*, *267*(1–2), 118–128. https://doi.org/10.1016/j.epsl.2007.11.042

Wang, K., Liu, Q., & Yang, Y. (2019). Three-dimensional sensitivity kernels for multicomponent empirical Green's functions from ambient noise: Methodology and application to Adjoint tomography. *Journal of Geophysical Research: Solid Earth*, *124*, 5794–5810. https://doi.org/10.1029/2018JB017020

Wang, K., Luo, Y., & Yang, Y. (2016). Correction of phase velocity bias caused by strong directional noise sources in high-frequency ambient noise tomography: A case study in Karamay, China. *Geophysical Journal International*, *205*(2), 715–727. https://doi.org/10.1093/gji/ggw039

Wang, K., Yang, Y., Basini, P., Tong, P., Tape, C., & Liu, Q. (2018). Refined seismic structure of Southern California by ambient noise adjoint tomography. *Geophysical Journal International*, *215*(2), 844–863. https://doi.org/10.1093/gji/ggy312

Wernicke, B. (1992). Cenozoic extensional tectonics of the U.S. Cordillera, in the Cordilleran orogen. *Geological Society of America*, 553–583. https://doi.org/10.1130/dnag-gna-g3.553

White, M. C. A., Ben-Zion, Y., & Vernon, F. L. (2019). A detailed earthquake catalog for the San Jacinto fault-zone region in Southern California. *Journal of Geophysical Research: Solid Earth*, *124*(7), 6908–6930. https://doi.org/10.1029/2019jb017641

Wilgus, J., Jiang, C., & Schmandt, B. (2020). A middle crustal channel of radial anisotropy beneath the northeastern Basin and range. *Tectonics*, *39*, e2020TC006140. https://doi.org/10.1029/2020TC006140

Xie, J., Ritzwoller, M. H., Brownlee, S., & Hacker, B. (2015). Inferring the oriented elastic tensor from surface wave observations: Preliminary application across the western United States. *Geophysical Journal International*, *201*(2), 996–1021. https://doi.org/10.1093/gji/ggv054

Xie, J., Ritzwoller, M. H., Shen, W., Yang, Y., Zheng, Y., & Zhou, L. (2013). Crustal radial anisotropy across eastern Tibet and the western Yangtze craton. *Journal of Geophysical Research: Solid Earth*, *118*, 4226–4252. https://doi.org/10.1002/jgrb.50296

Yan, Z., & Clayton, R. W. (2007). Regional mapping of the crustal structure in Southern California from receiver functions. *Journal of Geophysical Research*, *112*, B05311. https://doi.org/10.1029/2006jb004622

Yang, Y., & Forsyth, D. W. (2006). Rayleigh wave phase velocities, small-scale convection, and azimuthal anisotropy beneath Southern California. *Journal of Geophysical Research*, *111*, B07306. https://doi.org/10.1029/2005JB004180

Yang, Y., Ritzwoller, M. H., Lin, F. C., Moschetti, M. P., & Shapiro, N. M. (2008). Structure of the crust and uppermost mantle beneath the western United States revealed by ambient noise and earthquake tomography. *Journal of Geophysical Research*, *113*, B12310. https://doi.org/10.1029/2008JB005833

Yao, H., Beghein, C., & Van Der Hilst, R. D. (2008). Surface wave array tomography in SE Tibet from ambient seismic noise and two-station analysis-II, Crustal and upper-mantle structure. *Geophysical Journal International*, *173*(1), 205–219. https://doi.org/10.1111/j.1365-246X.2007.03696.x

Yao, H., & Van Der Hilst, R. D. (2009). Analysis of ambient noise energy distribution and phase velocity bias in ambient noise tomography, with application to SE Tibet. *Geophysical Journal International*, *179*(2), 1113–1132. https://doi.org/10.1111/j.1365-246X.2009.04329.x

Zandt, G., Gilbert, H., Owens, T. J., Ducea, M., Saleeby, J., & Jones, C. H. (2004). Active foundering of a continental arc root beneath the southern Sierra Nevada in California. *Nature*, *431*(7004), 41–46. https://doi.org/10.1038/nature02847

Zhao, D., Kanamori, H., & Humphreys, E. (1996). Simultaneous inversion of local and teleseismic data for the crust and mantle structure of Southern California. *Physics of the Earth and Planetary Interiors*, *93*(3–4), 191–214. https://doi.org/10.1016/0031-9201(95)03076-X

Zhu, H., Bozdağ, E., & Tromp, J. (2015). Seismic structure of the European upper mantle based on adjoint tomography. *Geophysical Journal International*, *201*(1), 18–52. https://doi.org/10.1093/gji/ggu492

Zhu, L., & Kanamori, H. (2000). Moho depth variation in Southern California from teleseismic receiver functions. *Journal of Geophysical Research*, *105*(B2), 2969–2980. https://doi.org/10.1029/1999JB900322

Zigone, D., Ben-Zion, Y., Campillo, M., & Roux, P. (2015). Seismic tomography of the Southern California plate boundary region from noise-based Rayleigh and Love waves. *Pure and Applied Geophysics*, *172*(5), 1007–1032. https://doi.org/10.1007/s00024-014-0872-1